Available online at www.sciencedirect.com
ScienceDirect
Computers & Fluids 37 (2008) 402–413
computers & fluids
www.elsevier.com/locate/compfluid

Prediction of sound generated by a rod–airfoil configuration using EASM DES and the generalised Lighthill/FW-H analogy

Björn Greschner [a,*], Frank Thiele [a], Marc C. Jacob [b], Damiano Casalino [c]

[a] Institute of Fluid Mechanics and Engineering Acoustics, Berlin University of Technology, Mueller-Breslau-Strasse 8, D-10623 Berlin, Germany
[b] Centre Acoustique du LMFA-UMR CNRS 5509, Ecole Centrale de Lyon 36, avenue Guy de Collonge, F-69134 Ecully, France
[c] Italian Aerospace Research Center (C.I.R.A.), Via Maiorise, 81043 Capua, Italy

Available online 27 February 2007

Abstract

Sound generated by an airfoil in the wake of a rod is predicted numerically by using a Detached-Eddy Simulation (DES) unsteady flow field and a Ffowcs Williams and Hawkings acoustic analogy formulation for the far field computation. Volume sources from the rod wake are found to play a non-negligible role at high frequencies and surface contributions might be flawed if the surfaces cross highly turbulent flow regions even if surrounding volume terms are accounted for. The DES approach is based on a novel cubic explicit algebraic stress turbulence model which is built on a two-equation k–ε model from Lien and Lechziner. This DES has been recently implemented at the Berlin University of Technology in the compressible Navier–Stokes flow solver *ELAN*. The aerodynamic results are compared to experimental data obtained at the ECL by Jacob et al., as well as to previous Large Eddy Simulations results from the Proust/Turbflow code by Boudet et al. and DES simulations from Greschner et al. based on standard turbulence models. The acoustic analogy is applied both with and without volume terms to rigid and permeable control surfaces surrounding the rod–airfoil system. Aeroacoustic results are compared to experimental data from the literature, showing that the inclusion of volume terms improves the aeroacoustic prediction in the broadband high frequency range.

1. Introduction

Recent studies have shown that the rod–airfoil test case is particularly suitable for the assessment of CFD codes in modeling broadband noise sources. The configuration is that of a symmetric airfoil located one chord downstream of a rod, whose wake contains both periodic and broadband vortical fluctuations. In particular, a significant broadening of the main Strouhal peak has been observed at subcritical vortex shedding conditions [1]. Since the intrinsic aeroacoustic capabilities of unsteady RANS and LES flow models have been fairly well understood, the further step consists in developing turbulence models for industrial applications that are able to reproduce broadband sound generation mechanisms with a reasonable computational effort. DES turbulence models restrict the LES domain to unsteady turbulent flow regions and use simpler closures elsewhere. They are expected to approach the quality of a LES prediction with optimised computational costs and are therefore a good candidate for this kind of applications, as shown by the authors in a previous paper [2]. However, DES is still in its infancy and undergoes continuing improvements. In the context of aeroacoustic predictions, this requires closer and closer comparisons between experimental and numerical noise spectra, the latter being obtained through a generalised Lighthill/FW-H acoustic analogy formulation [3,4] applied to the unsteady aerodynamic solution. In this approach, even at low Mach numbers, the volume sources due to free turbulent eddies may have a discriminative role in the assessment of different turbulence models. For this reason, the main concern of this paper is to shed light on

* Corresponding author.
E-mail addresses: Greschner@cfd.tu-berlin.de (B. Greschner), Thiele@cfd.tu-berlin.de (F. Thiele), Marc.Jacob@ec-lyon.fr (M.C. Jacob), D.Casalino@cira.it (D. Casalino).

0045-7930/$ - see front matter © 2007 Published by Elsevier Ltd.
doi:10.1016/j.compfluid.2007.02.013

Nomenclature

DES	Detached Eddy Simulation	y^+	dimensionless first-cell spacing
LES	Large Eddy Simulation	L_n	wall normal distance
RANS	Reynolds Averaged Navier–Stokes	u_i	components of velocity vector (fluid)
EASM	Explicit Algebraic Stress Model	v_i	components of the surface velocity
LL	Lien and Leschziner	$\mathrm{n_i}$	surface normal vector
DIT	Decay of Isotropic Turbulence	$\boldsymbol{v}$	velocity vector (fluid)
FW-H	Ffowcs-Williams and Hawkings	$\boldsymbol{\omega}$	vorticity vector
HWA	hot wire anemometry	ρ	density
FFT	Fast Fourier Transformation	a	speed of sound
PSD	power spectral density	p	pressure
Re	Reynolds number	k	turbulent kinetic energy
St	Strouhal number	ε	turbulent dissipation
Ma	Mach number	μ	molecular dynamic viscosity
Pr	Prandtl number	μ_t	eddy viscosity
Tu	turbulence intensity	v	kinematic viscosity
C_{DES}	model constant for DES	τ_{ij}	stress tensor
L_{DES}	turbulent length scale for DES	C_x, c_μ	constants for turbulence model
L_{RANS}	turbulent length scale for RANS	f	frequency
Δ	grid size	T_{ij}	Lighthill's stress tensor
d	rod diameter	δ_{ij}	Kronecker symbol
c	airfoil chord length	τ	retarded time ($[.]_{\mathrm{ret}}$)
R	distance to observer	S_n	enumerated surface ($n = 01$–05)
x, y, z	coordinates	V_n	enumerated volume ($n = 01$–08)

the influence of Lighthill's stress tensor in a hybrid DES/FW-H aeroacoustic simulation.

Several authors in the past (e.g. Refs. [5,6]) have taken advantage of the arbitrary nature of the integration surface in a FW-H formulation to avoid the expensive computation of volume contributions. The idea is to integrate the noise contributions from sources located both on physical surfaces and in the free flow by using a permeable integration surface that encompasses both the body and the most energetic vortical fluctuations. In the rod–airfoil case, for instance, this approach was applied by Casalino et al. [7] who showed that, for a low Mach number (<0.2) unsteady RANS simulation, the acoustic far field is not affected by the location of the integration surface. In other words, at low Mach numbers, a RANS-based tonal aeroacoustic prediction could be carried out without taking into account the volume source terms. Surprisingly, a different behaviour was observed by Boudet et al. [8] by performing LES computations of the rod–airfoil flow at comparable Mach numbers. In particular, discrepancies in the high frequency spectral components were observed between noise signals computed by using different, either solid or permeable, integration surfaces. Thus Casalino's results, obtained with the same codes as Boudet's but a different turbulence model, cannot be explained by the low Mach number. At least they are consistent with Boudet's results since the RANS prediction is purely tonal without any broadband content and the behaviour observed by Boudet et al. occurs in a high frequency broadband range.

There are two possible explanations for the behaviour observed by Boudet et al. The first one is that the spurious pressure fluctuations may be generated upon a permeable surface when a turbulent eddy crosses the surface because only part of it is taken into account for by the surface integration. Since quadrupoles may result from compensating dipoles, this non-physical sources may become quite efficient in some situations. The second explanation is that the volume sources themselves may contribute to the sound radiation and become significant at frequencies where surfaces sources are not so powerful. These two aspects can be checked by comparing sound computations from various integration surfaces. The numerical investigation of this behaviour is another goal of the present study.

Recent improvements of the DES turbulence models have been implemented in the flow solver *ELAN* [9] developed at the Berlin University of Technology. The advantages of the favoured cubic ESAM are the improved quality in the simulation of complex wall bounded flows using a two-layer RANS model and yet another point is the separated formulation of the DES modification (not influenced by the RANS model), that allows simplified implementations to avoid negative effects of the DES approach such as grid induced separation (GIS-shield) and the unphysical reduction of the eddy viscosity due to the activation of the low Reynolds number wall-damping terms in fine grid areas far away from the walls [10]. Moreover, the volume source terms have been included in the FW-H acoustic analogy predictions. These are the specific novelties of this paper with respect to the previous one [2]. The main emphasis is therefore placed on these novel features of the hybrid DES/FW-H aeroacoustic approach.

Section 2 is devoted to the description of the numerical approach and the flow configuration. Section 3 provides an overview of the aerodynamic results whereas Section 4 is specifically concerned with the sound computations. The conclusions are drawn in Section 5.

2. Simulation tools and flow configuration

2.1. ELAN flow solver

The unsteady aerodynamic field is computed by using an in-house finite-volume code that solves either the unsteady Reynolds averaged or spatially filtered Navier–Stokes equations employing a RANS or Large Eddy simulation, respectively. An implicit formulation is used with second order accuracy both in space and in time. All scalar quantities, as well as the Cartesian components of tensorial quantities are stored in the cell centres of arbitrarily curvilinear, semi-structured grids that can fit very complex geometries with the desired local refinement level. Linear momentum equations are solved sequentially, with the pressure field computed at each time step via a separate iterative procedure based on a pressure-correction scheme of the SIMPLE type with an additional compressible convection term as described by Ferziger and Peric [11]. The set of compressible equations is completed with an equation for the total enthalpy and the ideal gas law. A generalised Rhie and Chow interpolation is used to avoid an odd-even decoupling of pressure, velocity and Reynolds-stress components. The equation system are solved by an iterative method, the well-known Stone's SIP solver and the time integration is fully implicit of second-order accuracy.

2.2. DES turbulence model based on the cubic EASM LL k–ε model

Hybrid approaches based on the idea of combining RANS and LES turbulence models have become increasingly popular in recent years, since they require a reduced computational effort in comparison to genuine LES, while retaining much of the physical accuracy of the method. The basic concept of DES was published in 1997 [12] and was based on the popular Spalart–Allmaras (SA) one-equation turbulence model. The peculiarity of a DES approach consists in using a single turbulence model, which behaves like a subgrid-scale model in regions where the grid density is fine enough for a LES, and like a RANS model in regions where it is not. In order to achieve this, the length scale in the underlying turbulence model is replaced by the DES length scale:

$$L_{\mathrm{DES}} = \min(L_{\mathrm{RANS}}, C_{\mathrm{DES}}\Delta), \tag{1}$$

where C_{DES} is a model constant analogous to that of the Smagorinsky constant in LES. L_{DES} is the turbulence length scale of the background RANS model and Δ is an appropriate grid size, e.g. the cubic root of the cell volume. Therefore L_{DES} plays the role of an implicit filter width in a LES fashion, as is directly based on the local grid size. The main goal is to achieve a RANS simulation in the vicinity of solid boundaries, and LES in regions of massive flow separation outside of the boundary layer. Although the replacement of the length scale (1) in a RANS model is simple, there is a potential risk to activate the LES length scale where it is not desired or should be explicitly avoided. Another risk is to activate the modeling terms in inappropriate regions [13]. The constant C_{DES} is calibrated by simulating the decay of isotropic turbulence (DIT) as described in Ref. [14]. For a two-equation model, the turbulence length scale is based on local turbulence quantities, and appears in more than one term of the model equations. Although the standard approach consists in substituting this in the dissipation term of the k-equation, similarly to what is done in the precursor SA-DES model, some degree of freedom exists in the employment of model constants, as shown in Ref. [15]. Both a wall normal distance and a locally-determined length scale are used in the cubic EASM model. Since this is a non-standard DES method, a short description is given hereafter. However, for an exhaustive representation of the model equations, tensor representation and model constants, the reader is remained to Ref. [16].

Due to the fact that the non-linear part of the k–ε model is not modified by the DES implementation, attention can be confined to the background model of the cubic EASM. The transport equations for the LL k–ε model [17] read

$$\frac{\partial \rho k}{\partial t} + \frac{\partial(\rho k u_i)}{\partial x_i} = \rho P - \rho\varepsilon + \frac{\partial}{\partial x_i}\left[\left(\mu + \frac{\mu_t}{Pr_k}\right)\frac{\partial k}{\partial x_i}\right], \tag{2}$$

$$\frac{\partial \rho \varepsilon}{\partial t} + \frac{\partial(\rho \varepsilon u_i)}{\partial x_i} = \rho\frac{\varepsilon}{k}(\widetilde{C}_{\varepsilon 1}P - \widetilde{C}_{\varepsilon 2}\varepsilon) + \frac{\partial}{\partial x_i}\left[\left(\mu + \frac{\mu_t}{Pr_\varepsilon}\right)\frac{\partial \varepsilon}{\partial x_i}\right]. \tag{3}$$

In the above equations k is the turbulent kinetic energy, ε denotes the turbulent dissipation, u_i is the velocity component in the i-direction, ρ represents the fluid density, P is the production of turbulent kinetic energy and μ the molecular viscosity. The eddy viscosity is denoted by μ_t, and the Prandtl number by Pr. Unsteady and convective terms on the left-hand side of the equations are balanced by production, dissipation, molecular and turbulent diffusion on the right-hand side. The various terms have the following expressions:

$$\begin{aligned} &\widetilde{C}_{\varepsilon 1} = C_{\varepsilon 1}\left(1 + \frac{P'}{P}\right), \quad \widetilde{C}_{\varepsilon 2} = C_{\varepsilon 2}(1 - 0.3\mathrm{e}^{-Re_t^2}),\\ &P' = \frac{\widetilde{C}_{\varepsilon 2}k^{\frac{3}{2}}}{C_{\varepsilon 1}L_\varepsilon}\mathrm{e}^{-A_\mu Re_k^2}, \quad Re_t = \frac{k^2}{\nu\varepsilon}, \quad Re_k = \frac{\sqrt{k}L_n}{\nu},\\ &A_\mu = 0.00222, \quad L_\varepsilon = \kappa c_\mu^{\frac{3}{4}}L_n(1 - \mathrm{e}^{-0.263Re_k}), \end{aligned} \tag{4}$$

where the constants $C_{\varepsilon 1} = 1.44$, $C_{\varepsilon 2} = 1.92$ and $c_\mu = 0.09$ are those of the standard k–ε model. The LL k–ε model is based on the idea of a two-layer model in order to comply with turbulent length-scale constraints inherent to Wolfshtein's one-equation model [18]. This basic concept presents some advantages in a DES formulation, as discussed below. The DES modification is performed by replacing the dissipation term $\rho\varepsilon$ of Eq. (2) by the following length-scale dependent term:

$$\rho\varepsilon \rightarrow \rho \frac{k^{\frac{3}{2}}}{\min(L_{\mathrm{RANS}}; C_{\mathrm{DES}}\Delta)} \tag{5}$$

with the RANS-model length-scale

$$L_{\mathrm{RANS}} = \frac{k^{\frac{3}{2}}}{\varepsilon}. \tag{6}$$

In the original RANS model, the two constants $C_{\varepsilon 1}$ and $C_{\varepsilon 2}$ depend on the wall-normal distance L_n. This non-local quantity is treated as an additional length-scale similarly to that employed in the SA model. Such a dependence ensures that, far away from a wall, the standard k–ε model is used, i.e.,

$$\lim_{L_n \to \infty} \widetilde{C}_{\varepsilon 1} = C_{\varepsilon 1}, \quad \lim_{L_n \to \infty} \widetilde{C}_{\varepsilon 2} = C_{\varepsilon 2}. \tag{7}$$

This happens of course in regions where the DES modification is wished to become active, and the behaviour of Eq. (7) should not be disrupted by this. To ensure that, the wall-normal distance length scale is not replaced by the DES length scale (1), as done in the SA-DES model. A further advantage of this simple approach is that the low Reynolds number terms of a RANS model, designed to account for the wall proximity effects, are not affected by the DES modification.

2.3. Flow configuration

2.3.1. Reference experiment

An experimental investigation of the rod–airfoil configuration was carried out in the high-speed subsonic anechoic wind tunnel [1] of the Ecole Centrale de Lyon. A symmetric NACA0012 airfoil (chord $c = 0.1$ m) and a circular rod ($d/c = 0.1$) were placed in the potential core of a jet. The airfoil was located one chord-length downstream of the rod. Both bodies extended $30d$ in the spanwise direction and were supported by rigid smooth plates. The incoming velocity was 72 m/s with a turbulence intensity $\mathrm{Tu} = 0.8\%$. The corresponding rod diameter based Reynolds number Re_d was about 48,000, that of the chord length was 480,000 and the Mach number Ma is approximately 0.2.

2.3.2. Numerical setup

The computational grid extends over $180d$ in the streamwise direction, $120d$ in the cross-stream direction and $3d$ in the spanwise direction. The 2D grid shown in Fig. 1 is repeated at 30 spanwise locations, with a constant spacing $\Delta z = 0.1d$. The grid is composed of about 2.3 million cells with 224 points around the rod and 344 points around the NACA0012 in circumferential direction and grid coarsening in the external blocks. The first cell size normal to the wall in turbulent units is $y^+ < 1.5$. An adiabatic low-Reynolds no-slip condition is imposed on the solid boundaries. Non-reflecting conditions from Bogey and Bailly [19] are imposed on the farfield boundaries. The time step used in the aerodynamic simulation is 10^{-6} s.

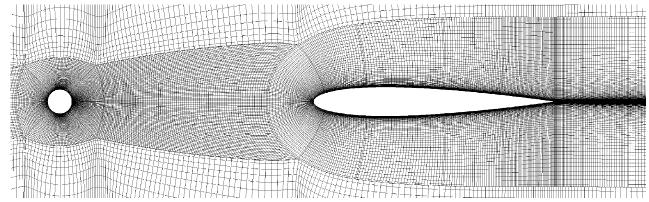

Fig. 1. 2D slice of computational grid.

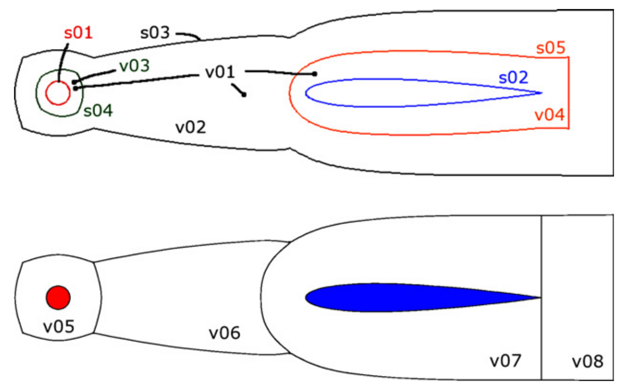

Fig. 2. Surfaces sXX and volumes vXX used for the acoustic analogy computation.

The integration surfaces and volumes used in the acoustic analogy computation are shown in Fig. 2. The acoustic results obtained by integration over either (S_{01} and S_{02}) or (S_{04} and S_{05}) are compared to those obtained by integration over (S_{03}) that encloses all the aeroacoustic sources, both with and without integrations in the corresponding outer volumes.

2.4. The FoxHawk aeroacoustic solver

The aeroacoustic computations are carried out by using the rotor-noise FW-H code *FoxHawk*. It computes the far field sound using a forward-time algorithm by Brentner [20] based on the well-known Formulation 1A by Farassat [21], extended to penetrable integration surfaces by Di Francescantonio [5] and Brentner and Farassat [6]. It is a generalization of the code *Advantia* described in [22] to generic body motions. The acoustic signals are calculated along with the aerodynamic field, saving both CPU-time and storage space. Indeed, since only a limited number of flow snapshots, contribute to the noise signal at a given reception time, previously computed flow snapshots can be progressively removed.

For the discussion of the FW-H algorithm the retarded-time formulation of the FW-H equation for the pressure p'

radiated into a medium at rest or in uniform motion by a flow in a region V around a surface or a set of surfaces S reads

$$4\pi \cdot p' = \frac{\partial^2}{\partial x_i \partial x_j} \int_V \left[\frac{T_{ij}}{r(1-M_r)}\right]_{\text{ret}} \mathrm{d}V - \frac{\partial}{\partial x_i} \int_S \left[\frac{L_i}{r(1-M_r)}\right]_{\text{ret}} \mathrm{d}S + \frac{\partial}{\partial t} \int_S \left[\frac{Q}{r(1-M_r)}\right]_{\text{ret}} \mathrm{d}S,$$

with

$$Q = \rho_0 U_i \hat{n}_i, \quad U_i = \left(1 - \frac{\rho}{\rho_0}\right) v_i + \frac{\rho u_i}{\rho_0}$$
$$L_i = P_{ij}\hat{n}_i + \rho u_i(u_n - v_n), \quad P_{ij} = (p - p_0)\delta_{ij} - \tau_{ij}$$
$$T_{ij} = \rho u_i u_j + (p' - a^2 \rho')\delta_{ij} - \tau_{ij}.$$

In the aeroacoustic literature, the three source terms are known as the quadrupole, loading and thickness noise source terms, respectively. The volumic quadrupole source term T_{ij} is the well known Lighthill stress tensor whereas the other source terms which are distributed over the integration surface, are due to induced fluctuations on the integration surfaces. In the most general situation, where a body is accelerated in a turbulent flow such fluctuations can be due both to incoming flow unsteadiness and to the unsteady motion of the surfaces (e.g. turbomachinery applications). The source terms in the brackets $[\ldots]_{\text{ret}}$ have to be evaluate at the retarded-time $\tau = t - |\boldsymbol{x} - \boldsymbol{y}|/a$, where $(\boldsymbol{x}, t)$ denote the observer position and time, $(\boldsymbol{y}, \tau)$ the source position and time, a the speed of sound in the medium at rest. The loading and thickness source terms are evaluated only on the surface S, where v_i is the velocity of the surface S and n_i is the surface normal vector. The Lighthill source term is evaluated for the region outside of the surface S (volume V). The algorithm implemented in *FoxHawk* is based on a slightly different but equivalent formulation: the space derivatives are transformed into time derivatives, the time derivative are moved into the integrals [6,21] and the forward-time formulation is used instead of the retarded-time formulation. The reason for choosing this formulation is that the classical retarded-time approach implies that the exact emission time of each source element has to be interpolated between two discretisation steps of the CFD simulation. This approach is less convenient from the numerical standpoint, since the acoustic computation has to be carried out *a posteriori* and requires massive storage of flow data. Conversely, a forward-time approach, as firstly proposed by Brentner [20], allows to carry out the acoustic computation along with the aerodynamic computation. The only restriction is that the observer positions have to be decided prior to the flow computation. For each source element $\boldsymbol{y}$ and for each discrete time τ at which the flow is computed the contribution to the observation point $\boldsymbol{x}$ is evaluated at the reception time $t = \tau + |\boldsymbol{x} - \boldsymbol{y}|/a$. Then, the pressure signals are interpolated at the observer location, which is much more accurate than a source interpolation. The complete description of the algorithm is detailed in Ref. [22].

Depending on the flow configuration, the FW-H algorithm can be applied in four different ways. The first approach is to compute only the loading and thickness terms on the rigid walls and to neglect the Lighthill source term. The formulation becomes much simpler and cheaper if applied to the walls and computational costs reduce accordingly. The error due to neglecting the Lighthill source term is small in the case of low Mach number and laminar flows. When strong shear layers exist in the flow or when the Mach number increases, the Lighthill term is not negligible anymore.

In this case a second approach is possible which consists in computing the contribution of all three types of sources directly (Lighthill, loading and thickness noise). Such an approach results in a very expensive volume source calculation. The direct calculation of the quadrupole noise together with the integration of the wall terms is in fact an exact reformulation of the Navier–Stokes equations and becomes an approximate solution of the noise radiation if the flow is surrounded by a medium at rest. The influence of the Lighthill term onto the quality of the broadband noise prediction for flows at moderate Mach number for real configurations (e.g. Landing gear) is not always clear. This issue has not been addressed very much because of the high computational costs that arise with the volume source computations. The calculations presented in this paper investigate this question for the rod–airfoil test case.

The third approach is to use a control surface that does not match the actual solid surfaces but that surrounds all bodies in the flow as well the most turbulent regions. The idea is that the fluctuations on this "permeable" surface are sources equivalent to the noise produced by all the sources (i.e. by the bodies and the volume sources) contained in the domain surrounded by the permeable surface. It is in fact a generalisation of Kirchhoff's approach to sources located in a turbulent flow, the great advantage being its validity if the flow crosses the integration surface as long as outer sources are properly accounted for. In this way the expensive computation of the volume terms is included in the far less expensive surface integrals of the FW-H approach. Although the permeable surface might be quite large in comparison to the solid walls, the gain with respect to volume integrations is of an order of magnitude. This gain explains why the "permeable" surface formulation has become so popular even in jet noise computations, that are mainly concerned with quadrupole noise. The influence of the location of the permeable surface on the predicted sound is not clear and a little bit tricky on real configurations. Indeed, when the surface is crossed by unsteady flows such as turbulent shear layers any other vortical flows, the integration might yield spurious noise. The reason is that original quadrupolar eddies are chopped as they cross the surface, since only the part that remains inside of the surface is taken into account. A quadrupole being a partial cancellation of two more efficient dipoles, the source strength is likely to increase during the crossing. This effect is not systematically observed however. Additionally this approach only works for compressible CFD codes with sufficiently low-dissipative schemes, because the code has to properly simulate the wave propagation through the volume enclosed by the permeable surface. Therefore the choice of the integration surface location is investigated in this paper for the rod–airfoil test case.

The fourth approach is to combine the permeable surface approach with the computation of Lighthill terms in the outer volume. This approach is only reasonable for research and educational aspects. In the present study it is expected to give an answer to the question raised by the third approach about noise generated by crossing eddies.

These four different approaches to the FW-H noise computations are undertaken in this paper to investigate the influence of the Lighthill source term on the predicted broadband noise for the rod airfoil test case. Results are validated against far field measurements.

3. Aerodynamics

The fully-developed three-dimensional vortical flow computed with the EASM DES model and a standard k–ε DES model from [2] are shown in Fig. 3. In both cases, a vortex shedding pattern can be observed downstream the rod, although strong spanwise effects prevent the formation of a regular Kármán vortex street. The non-dimensional shedding frequency for the EASM DES model is $St = 0.183$ (± 0.008, $\Delta f \sim 61$ Hz) and is very close to the experimental value of 0.19 and the numerical value of 0.185 obtained with standard k–ε DES model. A qualitative comparison of the vorticity iso-surfaces shows that the EASM DES model captures smaller turbulent structures than the standard model. A better aeroacoustic simulation in the high frequency range is therefore expected with this new model.

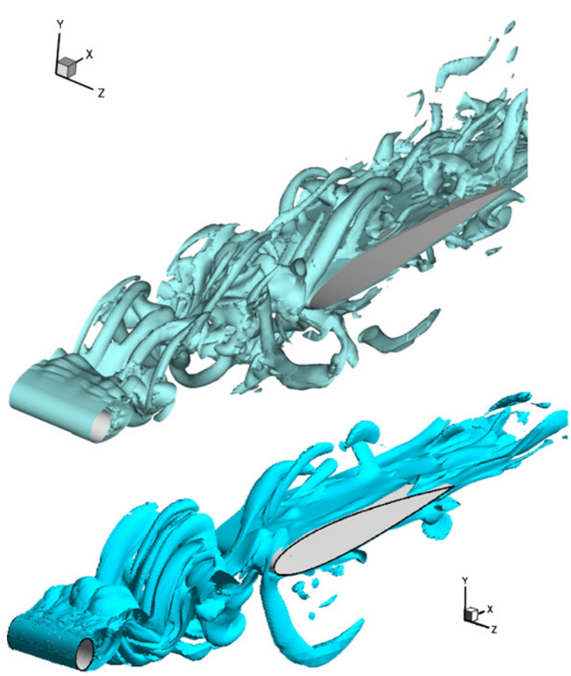

Fig. 3. Instantaneous vorticity iso-surfaces obtained through the EASM DES model (top) and a standard k–ε DES (bottom) [9].

In order to illustrate the spatial distribution of the aeroacoustic volume sources, the divergence of Prandtl's vortex force, i.e. div($\boldsymbol{\omega} \times \boldsymbol{v}$), is represented in Fig. 4. This term, on which the theory of Powell's vortex sound is based [23], is also a different form of Lighthill's quadrupole source term [24] for incompressible flows. This plot shows that the acoustic computation can be restricted to a region close to the rod–airfoil system. Fig. 5 shows mean- and rms-velocity profiles in the mid-span plane at the two cross-sections sketched on the top plot. The cross-section [A] is 0.255 chord upstream of the airfoil leading edge, that is, three quarter chord downstream of the rod whereas the cross-section [B] is a quarter chord downstream of the leading edge, near the thickest airfoil section. Present numerical results are compared to previous DES results [2], previous LES results by Boudet et al. [8] and to HWA experimental results by Jacob et al. [1]. The LES results from Boudet et al. were obtained with the compressible finite volume multiblock structured solver *Proust* now renamed *Turb'-flow*, using high order centred spatial schemes and 5th order Runge–Kutta explicit time advancement. The LES model is a modified Smagorinski model with a self-adaptative Smagorinski "constant" that is suited for wall flows. The mesh had about 2.3 Million points and was quite similar to the present one with slight differences in the central part. Slip boundaries were used in the spanwise direction where the flow extended over $3d$. More details are given in [8]. Previous DES simulations under-predict the fluctuating velocity in the near-wall region, due to the RANS model used in this area. Furthermore, the mean velocity profiles of the former DES simulations are not in a good agreement with the experiments, especially in the near wall region. Both the mean and fluctuating velocity profiles obtained by employing the EASM DES model are similar to the LES results by Boudet et al. [8] and quite close to

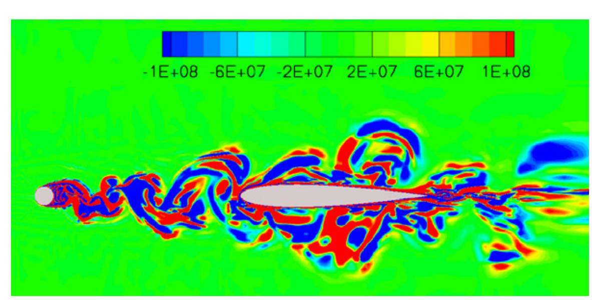

Fig. 4. Visualization of the divergence of Prandtl's vortex vector – div($\omega \times v$) (at mid-spane).

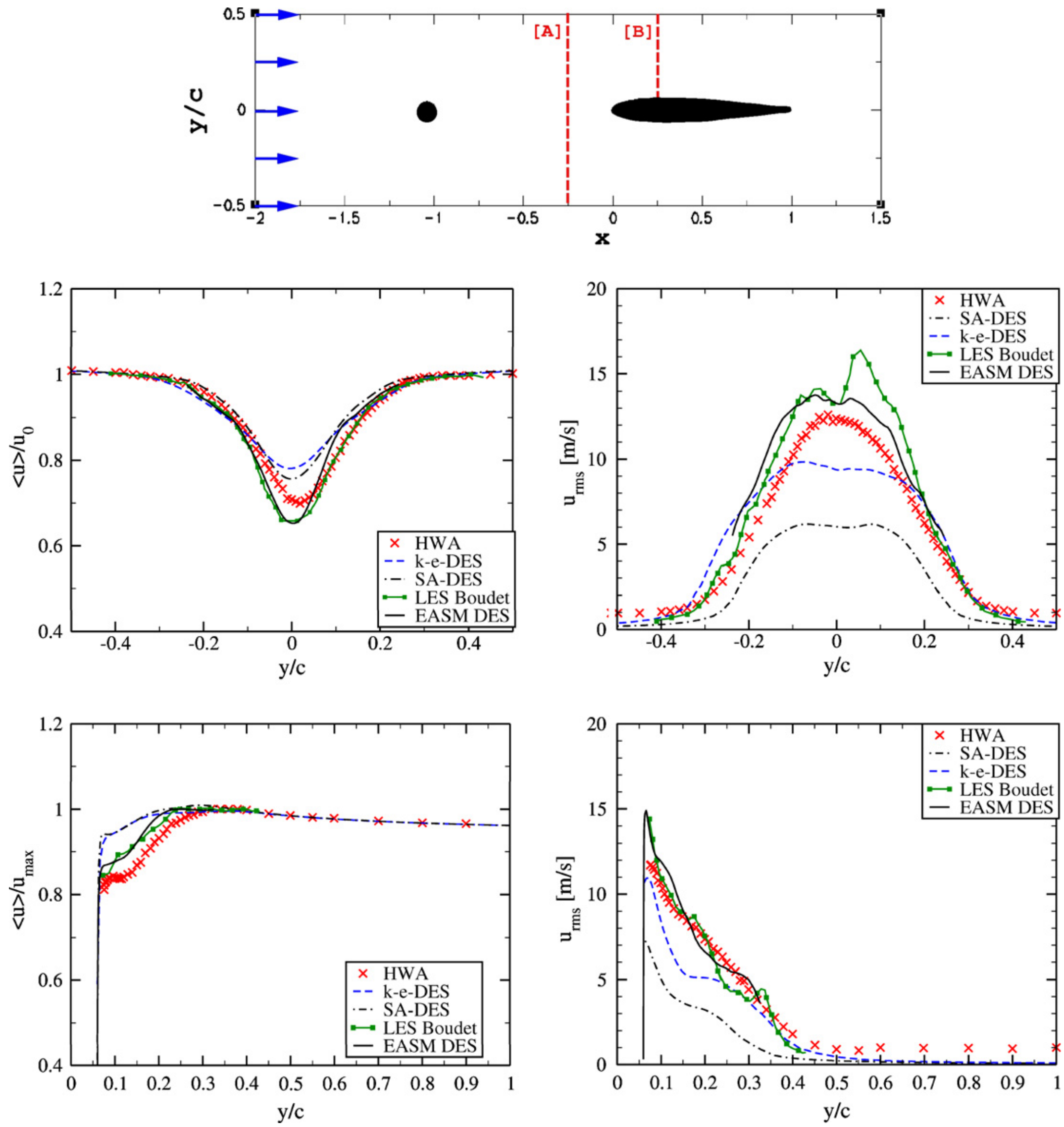

Fig. 5. Comparison of mean velocity and RMS value of velocity fluctuations to Hot Wire Anemometry (HWA) [13]; measurement positions (top), Position A (middle), Position B (bottom) – compared to [8,9].

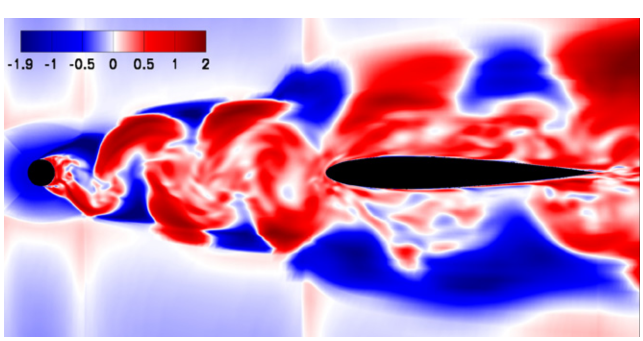

Fig. 6. Logarithm of the ratio of turbulent length scale of RANS model and DES grid scale $\log 10(L_{\mathrm{RANS}}/C_{\mathrm{DES}}\cdot\Delta)$, red – LES mode, blue – RANS mode.

the experimental data. The unsteady velocity prediction is significantly improved with the EASM model, in particular in the near wall region. In Fig. 6 the ratio of the RANS and LES turbulent length scales are compared on a snaphot. Actually, the logarithm of this ratio is plotted:

$$A = \log(L_{\mathrm{RANS}}/C_{\mathrm{DES}}\Delta).$$

In regions where A is positive the code switches to the "LES mode" (red) whereas it switches to "RANS mode" (blue) if it is negative. Regions where both length scales compete are coloured in white.

4. Acoustic results

The far-field noise is computed by applying the FW-H code to the five different integration surfaces (S_{01}–S_{05}) and to the four volumes (V_{01}–V_{04}) bounded by these five surfaces. Moreover, four additional integration volumes (V_{05}–V_{08}) are considered that form an alternative subdivision of

(V_{01}) as shown in Fig. 2. (V_{05}) contains (V_{03}) and surrounds the rod. (V_{07}) surrounds the airfoil but only partially covers (V_{04}) (it is larger in the cross-stream and upstream directions but ends at the airfoil trailing edge thus leaving a slice of (V_{04}) uncovered). (V_{08}) contains the whole region of (V_{01}) located downstream of the airfoil trailing edge (it covers the slice of (V_{04}) not covered by (V_{07}). (V_{06}) is the region comprised between (V_{05}), (V_{07}) and the surface (S_{03}). It contains most of the rod wake except for the near wake, and the vicinity of the airfoil trailing edge. The observer is located at a distance of 1.85 m from the airfoil mid-point, in a direction normal to the mean flow and to the airfoil chord in the mid-span plane. The far field is computed from 37,500 time steps, i.e. approximately 50 shedding cycles. All spectra are obtained by averaging 50 Fourier transforms carried out on 16,384 samples using a Hanning window (approximately 21 shedding cycles). This leads to a spectral resolution of $\Delta f \sim 61$ Hz. In order to compare the computed spectra to the experimental one that was obtained with a spectral resolution of 4 Hz, all results are expressed in terms of power spectral density (PSD). The simulated span of three diameters ($L_{\text{sim}} = 3d$) is less than the span of the test configuration ($L_{\text{exp}} = 30d$), therefore a scaling correction of $\Delta\text{PSD} = 8.2$ dB has been applied, as suggested by Kato [25]. The spanwise coherence length L_c on the rod surface is approximately equal to $2d$. The formula of Kato reads as follows:

$$\text{PSD}_{\text{exp}} = \text{PSD}_{\text{sim}} + 20\log(L_c/L_{\text{sim}}) + 10\log(L_{\text{exp}}/L_c).$$

The loading and thickness noise integrals will hereafter be considered as a single term referred to as ‘‘surface term’’ or ‘‘surface integral’’. The numerical acoustic results obtained by computing the surface integral on the solid surfaces (S_{01}), (S_{02}), (S_{01} and S_{02}), the volume integral of the surrounding volume (V_{01}) and the overall contribution of (S_{01} and S_{02} and V_{01}) are compared to experimental results in Fig. 7a and b. Both the single contribution of each integral term and their overall contribution are represented. Globally, the hybrid EASM DES/FW-H aeroacoustic results are in good agreement with the measurements in the whole broadband spectrum: the broadband noise levels are accurately estimated, as well as the level of the main peak at the shedding frequency. During the computation, results improved as the signals lengthened and the spectral resolution of the Fourier transforms increased. These results also show the improvement due to EASM model with respect to standard DES models (see Greschner et al., [2]): hence the better prediction of the unsteady flow features by the EASM model, makes a more accurate sound prediction possible. However the accuracy of prediction depends on the actual terms included in the prediction. Indeed, beyond 10 kHz the PSD is mainly determined by the volume sources (the green and the black curves in Fig. 7a are nearly identical and about 10 dB above the red and blue curves). Subsequently the predictions that include the volume integral are very accurate above 10 kHz (Fig. 7a) whereas the others are not (Fig. 7b). Note that the accuracy of the high frequencies can only be estimated up to the experimental frequency limit 12.8 kHz. In the lower frequency range the volume sources can be neglected and the surface source contribution (S_{01} and S_{02}) is close to experimental values. The relative contribution of each surface breaks down as follows: up to about 3 kHz, the airfoil contribution (S_{02}) dominates, between 3 and ~6 kHz, the rod (S_{01}) and the airfoil (S_{02}) contributions seem to compare as far as the statistical convergence makes it possible, and above 6 kHz, the rod (S_{01}) dominates. This is somewhat different from the experiment where the airfoil contribution is more than 10 dB above the rod contribution for all frequencies higher than a few hundred Hertz, and up to 6 kHz according to Jacob et al. [1]. Above 6 kHz, the experiment only tells that the rod contribution becomes of the same order as the overall contribution since the experiment does not offer the possibility to isolate the airfoil contribution. However this difference can at least partly be attributed to the lack of statistical convergence of the numerical computations that results in the jigsaws of the spectra. This first comparison clearly demonstrates how the volume terms improve the far field prediction in the high frequency range. This is rather surprising at such a low Mach number. In fact, since the dipole sound is mainly concentrated

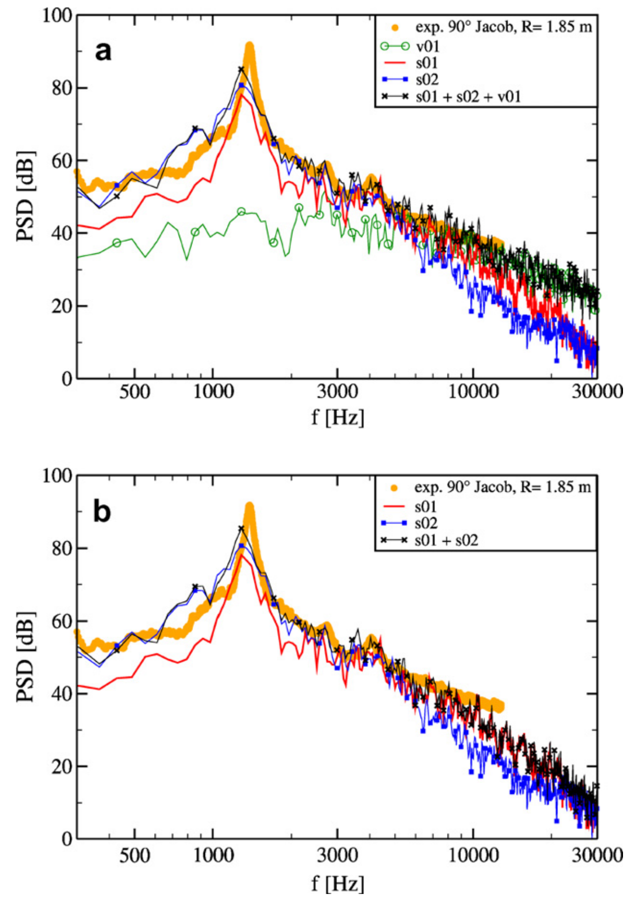

Fig. 7. Comparison of EASM DES/FWH to measurements of Jacob [13] for an observer ($R = 1.85$ m) normal to the flow.

at lower frequencies, the quadrupole sound becomes the only significant source in the high frequency range. Another interesting point is that at the rod shedding frequency the signals are nearly in phase and interfere constructively.

Fig. 8a shows again the result obtained from an integration on the body surfaces and on the surrounding volume (S_{01} and S_{02} and V_{01}), compared to that obtained from an integration on the surface (S_{03}) that surrounds (V_{01}). According to theory, the integration on the permeable surface (S_{03}) implicitly includes all the sound sources contained by the surface and should therefore yield the same result as the (S_{01} and S_{02} and V_{01}) integration. The results are indeed in good agreement, with a slight difference between 2 kHz and 6 kHz and in the very low frequency range (<700 Hz). Since the spurious noise radiated by eddies that cross the downstream face of (S_{03}) is expected at higher frequencies (Boudet et al. [8]), the remaining slight difference is probably due to the fact that the mesh of (S_{03}) is coarser than that of (S_{01}), (S_{02}) and the sound producing regions of (V_{01}). Nevertheless, this comparison

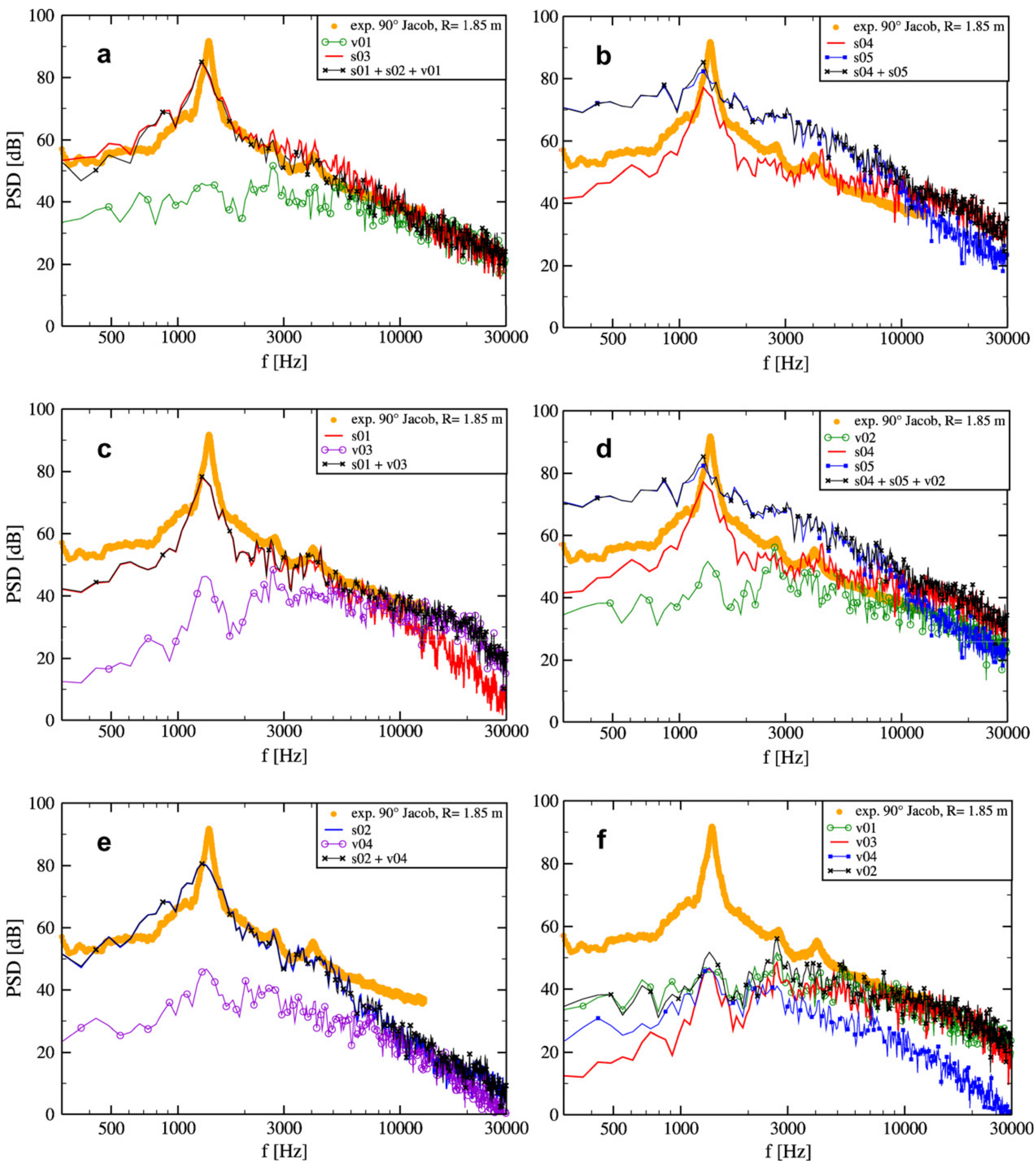

Fig. 8. Comparison of EASM DES/FWH to measurements of Jacob [13] for an observer ($R = 1.85$ m) normal to the flow.

confirms that the discrepancy between sound computed from solid surfaces (S_{01} and S_{02}) and permeable one (S_{03}) might be due to the neglected volume terms.

Figs. 8c and e show the noise contributions due to the rod and to the airfoil, separately, with and without the corresponding volume contributions. The red line in Fig. 8c represents the noise contribution of the rod surface (S_{01}), which is compared to the volume source contribution of the surrounding volume (V_{03}) (purple) with the near rod wake. The black line represents the overall rod contribution (S_{01} and V_{03}). It is clear that the volume contribution becomes significant at frequencies above 8 kHz, allowing a better agreement between numerical and experimental results. Interestingly, the volume contribution due to (V_{03}) is, in the range from 8 kHz to 20 kHz, of the same order than the contribution to the overall volume (V_{01}) as shown in Fig. 8f. This seems to infer that the dominant volume sources are located in the vicinity of the rod. Furthermore, a peak at the shedding frequency appears in the rod volume contribution. It is interesting to note however that this peak is relatively low with respect to the high frequency broadband content of the spectrum, considering that the wake starts from the quasi periodic vortex shedding. Similarly the airfoil contribution is plotted on Fig. 8e: the blue curve is the airfoil surface contribution (S_{02}), the purple represents the volume contributions from the vicinity of the airfoil (V_{04}), and the black curve shows the sum of the two contributions (S_{02} and V_{04}). The airfoil contribution plotted in Fig. 8e shows that, below 6 kHz, the spectral broadening of the main Strouhal peak is mainly due to the pressure fluctuations induced by the vortex shedding onto the airfoil surface whereas the contribution of the volume sources around the airfoil (V_{04}) is not significant. This volume source contribution does not become significant at higher frequencies, unlike the near rod wake contribution. Thus the dominant role of the rod near wake in the volume source radiation is confirmed. Figs. 8b and d show contributions of the permeable surfaces (S_{04}) and (S_{05}), surrounding the rod and the airfoil respectively, their sum (S_{04} and S_{05}), and the overall contribution (S_{04} & S_{05} and V_{02}), obtained by considering also the contribution of the volume (V_{02}). The acoustic result based on (S_{04} and S_{05}) seems to predict fairly well the shedding frequency, but the levels are overestimated in almost the whole frequency range. Differences up to about 15 dB with the contributions of (S_{01} and S_{02} and V_{01}) or equivalently (S_{03}) can be observed (see Fig. 8a). Thus the (S_{04} and S_{05}) result is obviously not physical. Apparently this discrepancy is related to the quadrupoles that cross the surface (S_{04} and S_{05}) and should thus be compensated by taking into account the volume terms surrounding this set of surfaces. This is done by adding the (V_{02}) contribution to that of (S_{04} and S_{05}) as shown in Fig. 8d: obviously the result is about 10–20 dB off from the (S_{03}) contribution (Fig. 8a) over the whole spectrum, except at the shedding frequency. A more detailed analysis shows that this overestimate is due to the (S_{04}) contribution in the lower and medium frequency range (up to 5 kHz), whereas it is due to (S_{05}) at higher frequencies. Since the (S_{03}) contribution matches very well the experimental data (Fig. 8a), it is accurate. For the same reason, the volume term computation in itself seems consistent since it has proven to play a positive role in the evaluation of the (S_{01} and S_{02} and V_{01}) contribution (Fig. 8a): thus (V_{02}) that is included in (V_{01}) must be quite accurate. As a consequence the contributions of the two permeable surfaces (S_{04}) and (S_{05}) are subject to spurious noise that is not compensated by outer volume terms. Therefore, the mismatch is necessarily due to the contributions of (S_{04}) and (S_{05}). This result is somewhat surprising since the contribution of the surface (S_{03}) which is also a permeable surface is quite accurate. The only reasonable explanation for this unexpected result is that the two surfaces (S_{04}) and (S_{05}) are crossed by much stronger unsteady flow patterns than the surface (S_{03}) is. Indeed the inflow and side boundaries of (S_{03}) are located in a quite region where the flow is almost steady and uniform. The only boundary of (S_{03}) that is crossed by an unsteady flow is the outflow boundary: this boundary is about a third chord downstream of the airfoil trailing edge where the flow perturbations are already damped. Conversely (S_{04}) and (S_{05}) cross the near wakes of the bodies they surround and (S_{05}) is crossed by strong eddies along all its sides. This might explain why the contribution of (S_{05}) is particularly far from expectations.

In Figs. 8f and 9a–c, the volume contributions of the various regions (V_{01} to V_{08}) illustrated in Fig. 2 are plotted. It is interesting to observe that the strength of the volume sources globally decreases in the streamwise direction. In fact, as shown in Fig. 9c, the airfoil volume contribution (V_{07}) is about 10 dB lower than the rod volume contribution (V_{05}), and the volume downstream of the airfoil (V_{08}) is 20 dB lower than the experimental levels.

To summarise these acoustic results, two main results can be highlighted. The first is that volume sources may play a role at low Mach numbers even if solid bodies are immersed in the flow. In the present case, it is shown that the quadrupole sources dominated the PSD at high frequencies where the surfaces sources do not contribute. The second result is related to the use of arbitrary control surfaces (or the so-called permeable surfaces) in the FW-H analogy: this study shows that the surface integrals may lead to erroneous sound estimates if they cross highly perturbed flow regions. In such cases even the outer volume sources do not compensate the spurious surface contributions. If expensive volume computations are to be avoided, there are only two types of candidates which are suitable for an accurate sound prediction using the FW-H analogy. Using the solid surfaces (S_{01} and S_{02}) or a permeable surface that surrounds all the major perturbed flow regions (S_{03}). The latter is better than the former since it implicitly accounts for the volume contribution that is not negligible in this flow. With the solid surfaces, this contribution is lost unless the Lighthill integral is computed. The high cost associated with the computation of Lighthill's volume

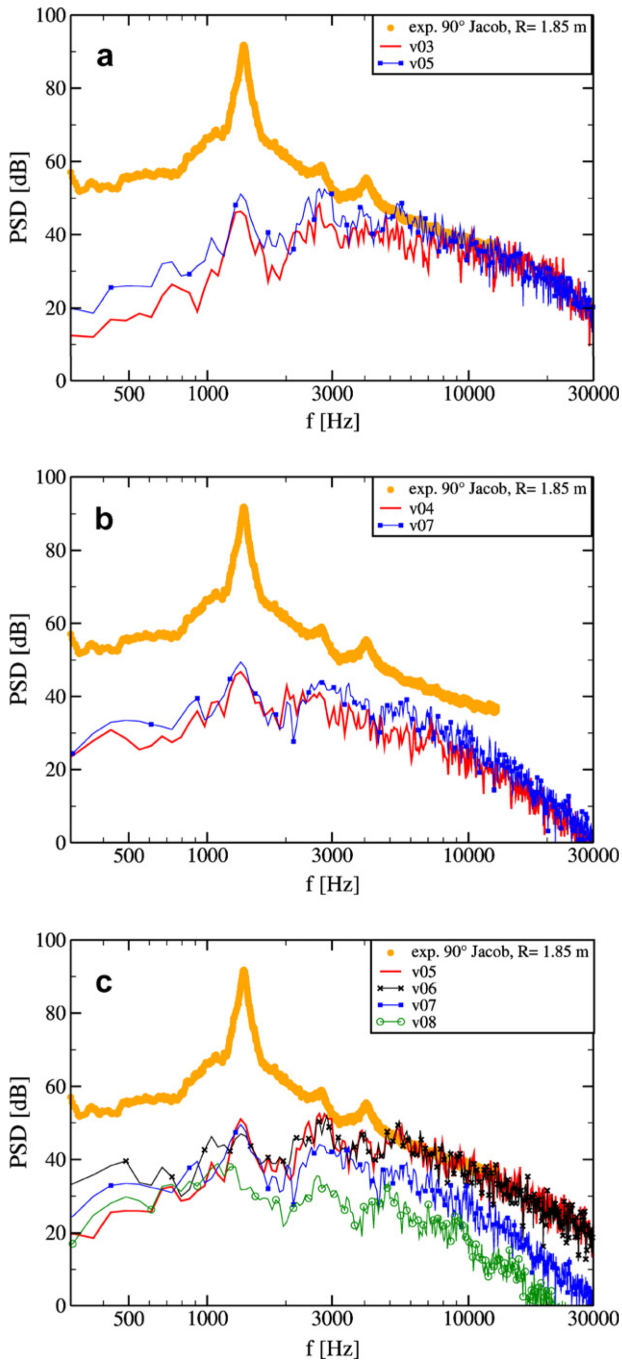

Fig. 9. a, b, and c. Comparison of EASM DES/FWH to measurements of Jacob [13] for an observer ($R = 1.85$ m) normal to the flow.

source term is the pitfall of this approach for real configurations.

5. Conclusions

The overall performances of a hybrid DES/FW-H aeroacoustic simulation chain have proven to be highly satisfactory in the prediction of broadband noise spectrum generated by a complex flow configuration. The new DES model offers a much more realistic flow picture than the standard k–ε DES. In Section 3, it has been shown that the EASM model improves the prediction of the unsteady flow features and reaches a quality that is comparable to LES. This is because the cubic ESAM turbulence model is more accurate in the wall regions than standard DES approaches. The spectral content of the flow, such as the broadening of the main Strouhal peak and the overall broadband spectrum, is well reproduced from cubic EASM DES simulation. Thus the DES predicts the main flow physics and turbulent scales of the rod wake, by adequately switching to the LES mode. As a consequence, it was found and discussed in Section 4 that its flow data is suitable for a very accurate sound prediction if the right integration surface is chosen (S_{03}).

The role of volume terms in the acoustic analogy formulation has been thoroughly investigated by considering various integration surfaces, both rigid and permeable ones, as well as a variety of integration volumes. The volume contributions generated by the Lighthill's sources in the near rod wake turn out to be significant in the high frequency range. When they are taken into account, the acoustic prediction is considerably improved in the high frequency range. Only two types of candidates which are suitable for an accurate sound prediction using the FW-H analogy by avoiding the expensive volume source calculation – the solid surfaces (S_{01} and S_{02}) or a permeable surface that surrounds all the major perturbed flow regions (S_{03}). The latter is better than the former since it implicitly accounts for the volume contribution that is not negligible in this flow. With the solid surfaces, this contribution is lost unless the Lighthill integral is computed (with high costs). A further interesting result is that integrations upon permeable surfaces yield unphysical results when the surfaces cross strongly perturbed flow regions. Their effect could not be compensated by including volume terms external to the permeable surface. Thus the application of the permeable surface approach to the FW-H sound prediction appears to be quite difficult in too highly turbulent flow regions. However, in quieter flow regions this approach gives excellent results and is a convenient way to avoid the costly computation of quadrupole sound.

Acknowledgement

This present joint French–German research work was partly supported by the German–French group "Noise generation in turbulent flows" from the DFG and the CNRS.

References

[1] Jacob MC, Boudet J, Casalino D, Michard M. A rod–airfoil experiment as benchmark for broadband noise modeling. J Theoret Comput Fluid Dyn 2005;19(3):171–96.
[2] Greschner B, Thiele F, Casalino D, Jacob MC. Influence of turbulence modeling on the broadband noise simulation for complex flows, AIAA Paper No. 2004-2902; 2004.

[3] Lighthill MJ. On sound generated aerodynamically. Proc Roy Soc Lond Ser A 1952;211:564–87.

[4] Ffowcs Williams JE, Hawkings DL. Sound generated by turbulence and surfaces in arbitrary motion. Phil Trans Roy Soc 1969;A264(1151):321–42.

[5] Di Francescantonio P. A new boundary integral formulation for the prediction of sound radiation. J Sound Vib 1997;202(4):491–509.

[6] Brentner KS, Farassat F. Analytical comparison of the acoustic analogy and Kirchhoff formulation for moving surfaces. AIAA J 1998;36(8):1379–86.

[7] Casalino D, Jacob MC, Roger M. Prediction of rod–airfoil interaction noise using the Ffowcs–Williams Hawkings analogy. AIAA J 2003;41(2):182–91.

[8] Boudet J, Grosjean N, Jacob MC. Wake-airfoil interaction as broadband noise source: a large-eddy simulation study. Inter J Aeroacoust 2007;4:93–116.

[9] Mocket C, Bunge U, Thiele F. Turbulence modelling in application to vortex shedding of stalled airfoils. In: Proceedings of the ERCOFTAC International Symposium Engineering Turbulence Modelling Measurements, ETMM6, Sardinia, Italy; 2005.

[10] Bunge U, Mockett C, Thiele F. Guidelines for implementing detached-eddy simulation using different models. Aerosp Sci Technol 2007;11:376–85.

[11] Ferziger JH, Peric M. Computational methods for fluid dynamics. 3rd rev. ed. Springer; 2002, ISBN 3-540-42074-6.

[12] Spalart PR, Jou W-H, Strelets M, Allmaras SR. Comments on the feasibility of LES for wings and on a hybrid RANS/LES approach. In: Proceedings of first AFOSR international conference on DNS/LES, 137-1-47; 1997.

[13] Spalart P, Deck S, Shur M, Squires K, Strelets M, Travin A. A new version of Detached-Eddy Simulation, resistant to ambiguous grid densities, Theor Comput Fluid Dyn [in press].

[14] Bunge U, Mockett C, Thiele F. Calibration of different models in the context of detached-eddy simulation. AG STAB Mitteilungen, DGLR, Göttingen; 2003.

[15] Yan J, Mockett C, Thiele F. Investigation of alternative length scale substitutions in Detached-Eddy Simulation. J Flow Turbul Combus 2005;74:85–102.

[16] Lübcke H, Rung T, Thiele F. Prediction of the spreading mechanism of 3D turbulent wall jets with explicit Reynolds-stress closures. Eng Turbul Model Exp 2002;5:127–45.

[17] Lien FS, Leschziner MA. Computational modelling of 3D turbulent flow in S-diffuser and transition ducts. Eng Turbul Model Exp 1993;2:217–28.

[18] Wolfshtein M. The velocity and temperature distributions in one-dimensional flow with turbulence augmentation and pressure gradient. Int J Heat Mass Transf 1969;12:301–18.

[19] Bogey C, Bailly C. Three-dimensional non-reflective boundary conditions for acoustic simulation: far field formulation and validation test cases. Acta Acoustica 2002;88:463–71.

[20] Brentner KS. A new algorithm for computing acoustic integrals. In: Proceedings of the 14th IMACS World Congress, July; 1994.

[21] Farassat F, Succi GP. The prediction of helicopter discrete frequency noise. Vertica 1983;7(4):309–20.

[22] Casalino D. An advanced time approach for acoustic analogy predictions. J Sound Vibr 2003;261(4):2003.

[23] Powell A. Vortex sound, Department of Engineering University of California, Los Angeles, Report No 61-70; 1961.

[24] Crow SC. Aerodynamic sound emission as a singular perturbation problem. Stud Appl Math 1970;49:21–44.

[25] Kato C, Iida A, Takano Y, Fujita H, Ikegawa M. Numerical prediction of aerodynamic noise radiated from low mach turbulent wake. In: 31st Aerospace Sciences Meeting and Exhibit; 1993.